Thermal Science and Engineering Progress 51 (2024) 102600

Contents lists available at ScienceDirect

Thermal Science and Engineering Progress

journal homepage: www.sciencedirect.com/journal/thermal-science-and-engineering-progress

Enhancing reliability and efficiency of solar chimney by phase change material Integration: An Experimental study

Ehsan Shabahang Nia, Mohsen Ghazikhani *

Department of Mechanical Engineering, Ferdowsi University of Mashhad, Mashhad, Iran

ARTICLE INFO

Keywords:
Solar chimney
Experimental results
Phase change material
Inorganic salt hydrate
Theoretical turbine
Performance analysis
Exergy efficiency

ABSTRACT

The Solar Chimney Power Plant (SCPP) presents an eco-friendly and straightforward technique for converting solar radiation into electricity. However, the performance limitations and reliability challenges of SCPPs are inherently linked to the variability and intermittency of solar radiation. To tackle this issue, using phase change materials (PCMs) can enhance the thermal energy storage and release capabilities of SCPPs. This study aims to explore the impact of PCM on the exergy efficiency and performance of a solar chimney. Two pilot solar chimneys with identical dimensions were constructed, each featuring a 4 m height chimney and a 5 m diameter collector. One solar chimney was equipped with hydrated salt PCM as an energy storage layer, while the other operated without PCM. Both systems' power production and ventilation potential were evaluated using theoretical turbines, and subsequent exergy analysis discerned the operational behavior and efficiency of the systems. Results indicate that PCM increased the average air mass flow rate through the solar system during the day. The average daily air mass flow rate was 0.045 kg/s with PCM and 0.033 kg/s without PCM. Notably, mean pressure drops resulting from the airflow through the turbine were 2.44 and 1.83 Pa in the presence and absence of PCM, respectively, over a complete day. Additionally, PCM improved exergy efficiency by about 19 % due to enhanced thermal energy storage.

1. Introduction

The accelerated depletion of finite fossil fuel reserves and the resulting environmental challenges have triggered a global shift towards cleaner and more sustainable energy sources. This necessity underscores the demand for renewable energy alternatives to address the growing global energy needs effectively. Solar energy stands out as a key contender among these alternatives, offering a reliable and widespread renewable resource. With its expansive and untainted power source, solar energy has played a significant role in meeting diverse energy requirements across various sectors, becoming a pivotal component of the renewable energy landscape. Numerous technologies have been developed to harness and convert solar energy into electrical power.

It is crucial to note that solar energy is subject to intermittent availability, unlike energy from finite fossil fuels. To bridge the gap between solar energy generation and its demand-driven utilization, the implementation of storage technology becomes essential. This approach ensures that surplus energy collected during periods of abundance can be stored for subsequent use during periods of reduced solar exposure, effectively addressing the intermittency inherent in solar energy sources. Utilizing solar energy, updraft towers operate by heating air beneath a solar collector, causing it to ascend towards the central chimney due to buoyancy. This heated air is then directed through a turbine to generate electricity.

Nevertheless, Solar Chimney Power Plants (SCPPs) encounter obstacles like high initial costs, substantial land requirements, suboptimal efficiency, and sporadic power output. Researchers propose overcoming these challenges by integrating phase change materials as agents for thermal storage or enhancement. PCMs, substances capable of absorbing or releasing latent heat during phase transitions, stand to enhance SCPP performance by augmenting the greenhouse's heat storage, refining heat transfer and tower airflow, extending operational durations, and curbing power output fluctuations. Incorporating PCMs into SCPP design, be it in the collector, the tower, or both presents opportunities to achieve heightened and more consistent power generation, reduce costs, minimize environmental impact, and improve synergy with other renewable energy sources.

The combination of a solar chimney and PCM is an innovative technology that has drawn many researchers' attention in recent years. Numerous investigations and studies have been done to examine the potential and benefits of this combination, as well as the challenges and

* Corresponding author.
E-mail address: Ghazikhani@um.ac.ir (M. Ghazikhani).

https://doi.org/10.1016/j.tsep.2024.102600
Received 4 February 2024; Received in revised form 19 April 2024; Accepted 26 April 2024
Available online 27 April 2024

Nomenclature

Symbols

A	Surface area (m^2)
c_p	Specific heat capacity at constant pressure (J/kg. K)
c_v	Specific heat capacity in constant volume (J/kg. K)
E_x	Exergy [W]
I_{global}	Global solar radiation (W/m^2)
$\dot{W}_{turbine}$	Turbine power output (W)
Q	Heat (W)
T	Temperature (K)
T_{ds}	Dead state temperature (K)
T_∞	Ambient temperature (K)
W	Watt
g	Gravitational acceleration (m/s^2)
H_{ch}	Chimney height (m)
R_{ch}	Chimney radius (m)
H_c	Collector height (m)
R_c	Collector radius (m)
V	Air flow velocity (m/s)
$\dot{m}$	Air mass flow rate (kg/s)
P	Pressure (Pa)
ke	Kinetic energy (kJ/kg)
z	Axial height of chimney (m)
$\dot{V}$	Volume flow rate (m^3/ s)
P_ν	Pressure difference (Pa)
h	Specific enthalpy (kJ/kg)
ρ	Density (kg/m^3)
R	Gas constant J/ (kg. K)
U	Overall heat transfer coefficient (W/m^2 K)
k	Specific heat ratio
r	Radius (m)

Greek letters

ε	Exergy efficiency
α	Absorptivity, roof absorption coefficient
η	Efficiency (%)
σ	Standard deviation

Subscripts

ds	Dead state
ch	Chimney
c	Collector
Exh	Exhaust
in	inlet
out	outlet

Acronyms

PCM	Phase Change Material
SC	Solar Chimney
SCPP	Solar Chimney Power Plant
CFD	Computational Fluid Dynamics
SALSCS	Solar Assisted Large Scale Cleaning System
FSCPP	Filter equipped Solar Chimney Power Plant
EOS	Equation of State
SUT	Solar Updraft Tower
EES	Engineering Equation Solver

limitations.

Gunther [1] first introduced the core principles underlying solar chimneys. The inaugural solar chimney power plant, standing at a height of 195 m, was erected in Manzanares, Spain. Following this, Schlaich and Haaf et al. [2–4] delved into an extensive analysis of SCPPs, covering aspects such as energy balance, design intricacies, and cost evaluations. Ming et al. [5] developed a set of mathematical models that describe the characteristics of the collector, chimney, and energy storage layer. These models were developed by thoroughly examining the influence of solar radiation on the energy storage layer.

Sharma et al. [6] were the first to introduce PCM modules in the solar chimney for natural ventilation. Their experiment utilized sodium sulfate decahydrate as the compound of choice. The researchers emphasized that storing PCM inside the solar chimney enables free nighttime ventilation without any additional cost as long as the PCM completely transforms from solid to liquid during the daytime. Xu et al. [7] conducted a numerical study investigating the relationship between solar irradiation and turbine pressure drop. They assessed how these factors affect the flow dynamics, heat transfer, output power, and energy losses in an SCPP. Peng-Hua et al. [8] conducted an independent study using three-dimensional numerical simulations. Their findings showed favorable outcomes regarding energy absorption and reduction in turbine pressure. Li et al. [9] performed a cost-benefit analysis on a reinforced-concrete SCPP, demonstrating substantial potential for real-world application. Safari and Torabi [10] incorporated PCMs into the solar chimney to improve its thermal efficiency, guaranteeing uniform temperatures and airflow rates throughout the watchroom. This entailed utilizing Phase change material as the thermal energy storage layer in the guardroom, efficiently controlling changes in temperature throughout the day.

Li and Liu [11] investigated a PCM-based solar chimney, examining heat fluxes at 500 W/m2, 600 W/m2, and 700 W/m2. They found complete PCM melting occurred only at 700 W/m2 despite maintaining a consistent 7-hour and 10-minute charge period. During the phase change process, variations in surface temperature remained consistent across all flux levels. Airflow rates correlated with surface temperature, peaking at 700 W/m2. However, air outlet temperatures were lowest at this level. Peak thermal efficiencies reached approximately 80 % for all cases during early ventilation, with the 500 W/m2 scenario demonstrating the highest minimum efficiency at 63 %.

Nasirivatan et al. [12] scrutinized the impact of corona wind on heat transfer within the SCPP absorber, revealing a notable 14.5 percent augmentation in heat transfer. Shabahang-Nia et al. [13] utilized flow control barriers on the absorber to augment both heat transfer and chimney inflow velocity. Ikhlef et al. [14] examined a small-scale SCPP with a thermal storage system in their study. They measured the chimney height to be 4.2 m, the diameter to be 0.24 m, and the collector diameter to be 5.93 m. Multiple thermal storage solutions were evaluated, and it was found that the basement with crushed gravel demonstrated the best level of performance, with a collector efficiency of 89.73 %. In their study, Liu-Bin et al. [15] examined how PCM displacement affects hybrid walls' performance.

Li et al. [16] examined the thermal behavior of a solar chimney power plant (SCPP) by utilizing a PCM called RT-42. They analyzed the impact of RT-42 at different degrees of heat flux. The primary purpose of this investigation was to evaluate the impact of the phase transition process on the temperature differential between the intake and output, as well as the pace at which mass flows. Benli and Durmus [17] investigated the thermal efficiency of $CaCl2\cdot H2O$ as a PCM in constructing a solar collector. In their study, Baby and Balaji [18] investigated pin–fin heat sinks by assessing the thermal performance using two distinct phase change materials. They also analyzed how different pin–fin topologies affected the efficiency of the heat sink. In addition, heat transmission efficiency was assessed at various volume fractions of PCM.

Rezaei et al. [19] examined the impact of PCM melting points on energy and exergy efficiency, as well as the corresponding energy and exergy costs for each PCM. Fadaei et al. [20] performed an experiment on a prototype SCPP that utilized paraffin wax as the PCM. The system consisted of a 3-meter chimney and a 3-meter collection. The results indicated that including PCM caused an elevation in absorber temperatures and augmentation in airflow velocity, leading to an enhancement of 8.33 % in mass flow rate and overall system efficiency. Bin et al. [15,21] examined how the thickness of PCM affects the efficiency of SCPP. The researchers determined that an increase in the thickness of the PCM resulted in the identification of a temperature peak. The researchers also examined the impact of PCM placement and observed that locating it in front of the absorber led to greater airflow temperatures compared to placing it behind.

Li et al. [22] developed a validated numerical model to examine how different parameters affect a solar chimney with PCM. According to their PCM thermal performance investigation, the phase change temperature significantly affects melting/freezing duration, air flow rate, and temperature differential. A greater temperature differential causes earlier complete melting, but ambient temperature changes may also induce it. Specific heat affects a material's sensible heat contribution. Increased thermal conductivity from 0.2 to 0.6 W/m·°C leads to a higher mass flow rate and temperature difference. After the early period, PCM temperature has no effect on melting. Bashirnezhad et al. [23] examined three separate cases to see how PCM affected the efficiency of solar collectors and photovoltaic panels. These scenarios involved using natural soil, water-filled black tubes, and paraffin-filled black tubes as thermal absorbers. The utilization of water and paraffin led to a respective enhancement in efficiency of 6.2 % and 22 %.

Thantong et al. [24] employed PCM in a SCPP to improve the natural ventilation process and reduce the amount of heat gained. Mounting PCM on the inside wall of the room resulted in lower temperatures inside, in contrast to the higher temperatures observed with concrete walls. In their study, Ebrahimnataj-Taiji et al. [25] performed a simulation of an SCPP that included a PCM and a finned absorber. They emphasized that utilizing PCM as a storage medium enabled constant temperature regulation throughout the area. Fins were considered essential for attaining thermal equilibrium inside the heat storage system of the phase change material. Chen and Chen [26] introduced a novel SCPP system that utilizes heat-saving sieve-plate beds filled with PCM capsules. Their investigation highlighted the substantial influence of the bed's permeability and the particles' size on the system's thermal efficiency. The augmentation of bed porosity from 0.4 to 0.6 resulted in improved convection heat transfer and elevated airflow temperatures, leading to a higher bed temperature at 0.6 porosity than 0.4.

Aligholami et al. [27] utilized energy and exergy analysis to examine geometrical parameters and introduced hydrophobic surfaces as a new method to improve the performance of Solar Chimney Power Plants. The study conducted an optimization of the functional diameter, height, and turbine pressure jump, taking into account the rate at which improvements can be made and the clarification of the optimization factor. The results highlighted the need of analyzing geometrical parameters together and demonstrated that including hydrophobic surfaces led to an 11 % performance improvement by decreasing shear stress. Pahamli and Valipour [28] investigated the utilization of PCMs in cold storage for food preservation appliances, encompassing refrigerators, freezers, refrigerated truck trailers, and display cabinets. PCMs, renowned for their high latent heat of fusion and narrow temperature range, offered energy-efficient solutions. Various thermal storage techniques and materials were discussed by the authors, addressing the low thermal conductivity of PCMs. They proposed enhancement methods such as fins, extended surfaces, PCM-embedded metal foams, nanoparticles, and Multiple PCM method techniques. Furthermore, the paper summarized and tabulated research findings on the application of cold storage materials in food preservation devices for easy reference.

Shojaeefard et al. [29] enhanced the performance of an isothermally heated horizontal capsule containing PCM for thermal energy storage. Their improvements included augmenting the PCM's low thermal conductivity through the incorporation of MgO and hybrid Ag/MgO nanoparticles and utilizing multilobed capsules. Employing the lattice Boltzmann method (LBM), they analyzed the nanoparticle effects on melting time. The study concluded by recommending the utilization of multilobed capsules to mitigate thermal conduction resistance. Rezaei et al. [30] conducted a study to enhance the efficiency of the solar chimney by implementing metallic tubes suspended within the collector. To assess the effectiveness of this modification in optimizing heat transport and enhancing system performance, they integrated computational fluid dynamics (CFD) models with empirical investigations. This novel design alteration resulted in a notable efficiency improvement, as evidenced by the valuable insights gleaned from the models and experiments. Atia et al. [31] examined the influence of different forms of absorber surfaces on solar chimney power plants. Different shapes, including triangles, rectangles, and semi-circles, were studied numerically. The results highlight the significant influence of a rectangular absorber, with up to a 67.4 % improvement in power output when its height is increased to 7.5 cm compared to a flat-chimney baseline. These insights aid in designing more efficient solar chimneys.

Corcione et al. [32] introduced an enhanced solar chimney system with four arrays of cylindrical absorber elements to increase efficiency and airflow rates. Their model considered radiative heat transfer and various convection modes. Results demonstrated superior performance compared to traditional systems, achieving up to 61 % efficiency and higher airflow rates. The proposed system also exhibited lower power losses, showcasing significant advantages over existing solutions. Further research is recommended to optimize convection modes and cylinder arrangements. Yoo et al. [33] propose the Filter-equipped SCPP, a hybrid of SCPP and Solar-Assisted Large-Scale Cleaning System (SALSCS) for simultaneous electrical power generation and outdoor air purification. Numerical simulations reveal higher energy consumption at the filter, with FSCPP's power generation at 20–40 % of SCPP. However, air purification capabilities closely match SALSCS with only a 2–4 % reduction. The FSCPP shows enhanced capabilities with increased solar chimney dimensions, offering a balance between power generation and air purification. Abdelsalam et al. [34] propose an innovative twin-chimney solar power plant design that outperforms traditional models. The solar chimney integrates a secondary chimney for enhanced water desalination, generating 1,111,754 kWh annually—2.9 times more than traditional designs.

Huang et al. [35] conducted experiments on a solar chimney's thermal performance with and without PCM at different inclination angles (30°, 45°, and 60°). They found that a 45° inclination provided optimal results, prolonging PCM melting times while achieving the shortest solidification time. Integration of PCM extended ventilation duration by over 10 h post-heat withdrawal, even at low heat fluxes of 200 W/m2 during diurnal cycle operation.

Chen et al. [36] conducted numerical and experimental studies to analyze natural convection heat transfer in a prismatic roof with a perforated partition and phase change material. They aimed to provide energy-saving solutions for passive building design. They investigated the effects of tilt angle, partition perforation size, and paraffin volume on flow dynamics. The zero-equation turbulence model was found to have the lowest error rate when compared with empirical formulas. Results indicated a 10 % increase in heat convection coefficient at larger inclination angles, with partition perforations inducing a chimney effect and noticeable updrafts.

Kim et al. [37] investigated incorporating a canopy-attached divider structure to enhance the thermo-fluid dynamic efficiency of solar updraft towers (SUTs). This structure aimed to emulate traditional vestibules, thereby improving thermal performance. Through computer simulations, various divider geometries were analyzed, revealing the potential for increased outlet velocity by up to 6.97 % when integrating the vestibule concept with SUTs. This study underscores the synergistic relationship between conventional architectural principles and innovative SUT designs.

Shabahang Nia et al. [38] developed a pilot SCPP with a 4 m chimney and 5 m collector. They utilized the data obtained from it as a basis for validating the simulations performed and subsequently conducted numerous simulations to optimize the dimensions of the system. Configurations with a 5 cm collector height showed the maximum velocity values, reaching the highest power output of 1.74 W with a 15-cm-high collector entrance and a 0.4-m chimney radius.

This research investigates the utilization of phase change materials to enhance the performance of solar chimney systems, considering regional climatic conditions. This study's outcomes can be a promising foundation for future research endeavours. Additionally, the innovative application of a theoretical turbine to assess the efficiency and performance of the system, along with the potential for expanding and refining this concept in systems with diverse dimensional and environmental conditions, is discussed. Employing a theoretical turbine for precise behavior tracking, the study calculates and compares exergy losses and efficiency in two cases: one with a PCM layer and one without. The study specifically highlights using a hydrated salt PCM, an inorganic material strategically positioned as a thermal storage layer beneath the collector. The results emphasize the potential advantages of integrating PCM into solar chimneys, highlighting enhancements in both performance and reliability.

2. 2. Experimental Setup

This study details the development of two solar chimneys (SCs) in Zanjan, Iran, each featuring a 5-meter diameter collector and a 4-meter chimney (refer to Fig. 1). The dimensions of the SCs were meticulously determined through a rigorous assessment balancing power generation efficiency, cost-effectiveness, and structural feasibility. Building upon insights obtained from a previous publication [38], which utilized a combination of experimental and numerical data, the dimensions of the system were refined to harmonize with these critical factors. The final dimensions of the SCs are presented comprehensively in Table 1. The collector architecture comprises a 5-millimeter-thick transparent glass canopy mounted on a robust metal structure, strategically designed to optimize solar radiation exposure on the absorber surface and induce a potent greenhouse effect. The tower's structural framework comprises a 4-meter PVC pipe with a 4-millimeter thickness. The pipe was chosen for its lightweight construction, durability, and heat resistance. To further augment solar radiation absorption and airflow temperature, the lower section of the absorber is coated with black paint.

Table 1
Configuration of SCs.

Dimension (m)	Symbol	Components
4	H_{ch}	Tower height
2.5	R_c	Collector radius
0.2	R_{ch}	Chimney radius
0.1	H_c	Inlet height

2.1. Measurement procedure and instrumentation

Various sensors were utilized to measure the temperature, velocity, and pressure of the airflow at both the inlet and outlet points of the system. The sensor arrangement is depicted in Fig. 2. It is important to highlight that the schematic representation of the embedded sensors in Fig. 2 is limited to only a quarter of the cross-sectional area of the solar chimney.

In each quadrant of the circular collector, a systematic integration of 8 SMT-160 temperature sensors has been implemented. Specifically, five of these sensors (S1-S5) are strategically positioned at intervals of 0.2, 0.5, 1.5, 2, and 2.5 m below the collector, enabling precise measurement of airflow temperature. Additionally, within each defined section, an additional set of 3 sensors (S6-S8) has been deployed to meticulously monitor the temperature on the absorber floor beneath the collector. This comprehensive sensor arrangement ensures thorough and accurate data collection, facilitating a comprehensive analysis of the system's thermal dynamics. Airflow velocity was measured using a hotwire anemometer (Lutron, YK2004AH), and BOSCH BMP180 sensors were employed to measure inlet and outlet airflow pressure in the solar

Fig. 1. SCs with and without PCM.

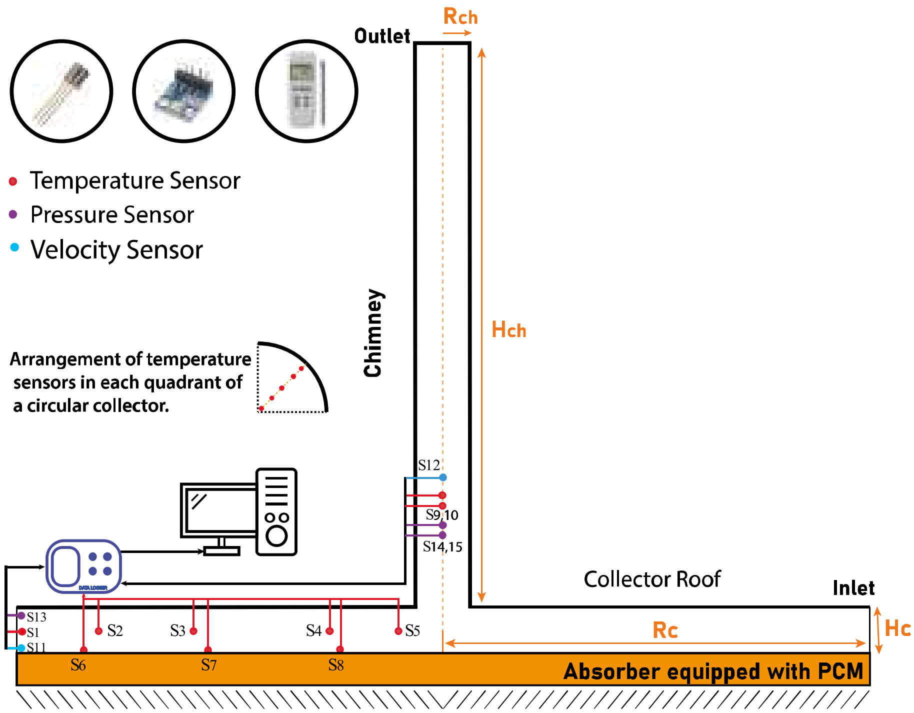

Fig. 2. Schematic depiction of SC and sensor arrangement.

chimney. It is noteworthy that the spatial positioning of all sensors in both setups is approximately consistent, with every effort made to minimize their impact on fluid flow. Further details regarding sensor accuracy and operational range can be found in Table 2.

2.2. Uncertainty analysis

An investigation into uncertainty was conducted to ascertain the accuracy of both primary and secondary parameters obtained. Upon analyzing a series of readings from a designated instrument, it was observed that individual measurements displayed nuanced discrepancies. Consequently, the researcher needed to calculate the mean of all readings to ensure accurate computations. Utilizing the notation x_i to represent each reading and with a total of n readings, the determination of the arithmetic mean (x_m) proceeded as follows [39]:

$$x_m = \frac{1}{n}\sum_{i=0}^{n} x_i \tag{1}$$

The definition of the deviation for each reading is $d_i = x_i - x_m$. The calculation of the standard deviation (σ) is as follows:

$$\sigma = \sqrt{\frac{1}{n}\sum_{i=0}^{n}(x_i - x_m)^2} \tag{2}$$

Table 2
Technical definitions of measuring devices.

Sensor Type	Model	Range	Accuracy	% Uncertainty
Temperature (S1-S10)	SMT-160	−45 to + 130 °C	± 0.7 °C	± 0.87
Air flow velocity (S11, S12)	Lutron, YK2004AH	0.2–20 m/s	<0.1 m/s + 5 % from reading	± 0.72
Pressure (S13-S15)	BOSCH BMP180	0—110000 N/m^2	±0.3 % of full-scale reading	± 1.045

Here is the definition of the standard deviation of the mean (σ_m):

$$\sigma_m = \frac{\sigma}{\sqrt{n}} \tag{3}$$

The recorded data's uncertainty or error is denoted by $\pm\ \sigma_m$. Table 2 provides the total uncertainty values.

3. Phase Change Materials (PCMs)

Phase Change Materials are pivotal in thermal energy storage and temperature regulation, facilitating heat absorption and release through endothermic melting and exothermic solidification processes. Selecting the appropriate PCM entails a comprehensive assessment of its kinetic, chemical, and thermophysical properties alongside environmental sustainability and economic viability considerations. PCMs are broadly categorized into eutectic, organic, and inorganic groups, each presenting limitations requiring careful consideration in equipment design. Inorganic PCMs are subdivided into salts, salt hydrates, and metallic PCMs. Notably, salt hydrates stand out within the PCM classification due to their remarkable attributes, including a high latent heat of fusion per unit volume, superior thermal conductivity compared to paraffin, and minimal volumetric changes upon melting, rendering them particularly noteworthy for various applications.

Many studies have been conducted on applying different phase change materials in the solar chimney, some of which can be summarized in Table 3. [56].

This study employed salt hydrate as a phase change material to investigate the system's efficiency and power output at different times of the day, as illustrated in Fig. 3. One of the collectors had the PCM positioned beneath its absorber to examine its influence on the performance of the solar chimney (SC). Several Sensors were used to conduct continuous measurements of temperature and velocity.

The PCM, totaling 80 kg, was packed in thin sealed plastic bags and evenly arranged beneath the absorber (Fig. 1). To ensure the uniform distribution of heat and minimize the impact of the geometric structure of the PCM-containing bags on airflow patterns, thin black polycarbonate sheets are used to cover them (while maintaining the

Table 3
The studies conducted on phase change material applications in solar chimneys.

Sources	PCM	Method
Sharma et al. [6]	Na2SO4 10H2O	Experimental
Li [46]	Paraffin Wax	Numerical and Experimental
Safari and Torabi [10]	Sodium sulphate decahydrate Na2SO4_10H2O	Numerical
Li and Liu [11]	Paraffin Wax RT42	Experimental
Li and Liu [16]	RT-42	Numerical
Liu and Li [47]	Paraffin RT42	Experimental and numerical
Li et al. [48]	Paraffin Wax RT 42	Experimental
Ismaeel et al. [49]	Paraffin Wax	Experimental
Murtadha et al. [50]	Paraffin Wax	Experimental and Numerical
Li et al. [22]	RT42	Numerical
Bin et al. [15,21]	Na2CO3·.10H2O	Experimental
Frutos Dordelly et al. [51–53]	Paraffinic RT44	Numerical and experimental
Bashirnezhad et al. [23]	Paraffin	Experimental
Fadaei et al. [20]	Paraffin wax	Experimental
Thantong et al. [24]	Paraffin wax	Experimental
Xaman et al. [54]	Paraffin wax 46_50	Numerical
Ochiai et al. [55]	Sodium sulfate decahydrate	Numerical
Ebrahimnataj Tiji et al. [25]	Sodium sulphate decahydrate (Na2SO4_10H2O)	Numerical
Chen and Chen [26]	Paraffin	Numerical

collector's height). The technical and thermophysical properties of the inorganic salt hydrate are detailed in Table 4, summarizing both test results and manufacturer-provided information.

To ascertain essential properties such as melting and freezing points, as well as other thermophysical characteristics of the phase change material under investigation, sensors housed within a variety of sealed plastic packages continuously recorded its instantaneous temperature. The data recorder collected these temperature readings at various intervals throughout both day and night, as demonstrated in Fig. 4. A comprehensive presentation of the test results, including relevant manufacturer details, is delineated in Table 4.

4. Mathematical Model

The central focus of this investigation is to explore the influence of incorporating Phase Change Material on the ventilation intensity and overall system performance during day-night cycles. To evaluate these aspects, a key method involves estimating ventilation intensity and power output using a theoretical turbine. The study employs a comprehensive metric, assessing power production over time for both system configurations (with and without PCM). Notably, the laboratory setups for both configurations were devised without the presence of an actual turbine, leading to the requirement for theoretical estimates of turbine output power. In response, a theoretical turbine is conceptualized within the solar chimney systems, as depicted in Fig. 5. Following this, the thermophysical properties and fluid flow characteristics of the system are thoroughly computed for this modified configuration. The next step entails computing and conducting a comparative analysis of output power and exergy efficiency for both system configurations. This methodological approach aims to elucidate the nuanced effects of PCM on ventilation dynamics and the overall performance of solar chimney systems.

4.1. One-dimensional modelling of SC

The modeling was carried out using the Engineering Equation Solver

Table 4
Thermophysical and technical characteristics of the PCM in use.

PCM Properties	Description
Primary Components	Inorganic Salt Hydrate + Water
Inflammability	No
Toxicity	No
Corrosion	No
Phase Change Melting Temperature (°C)	32–35
Thermal Conductivity (W/m/°C)	0.7 ± 15 %
Latent Heat (J/cm^3)	425
Approximated Specific Heat (J/gr/°C)	6.04
Specific Gravity (gr/cm^3)	1.47
Super Cooling (°C)	3 to 5

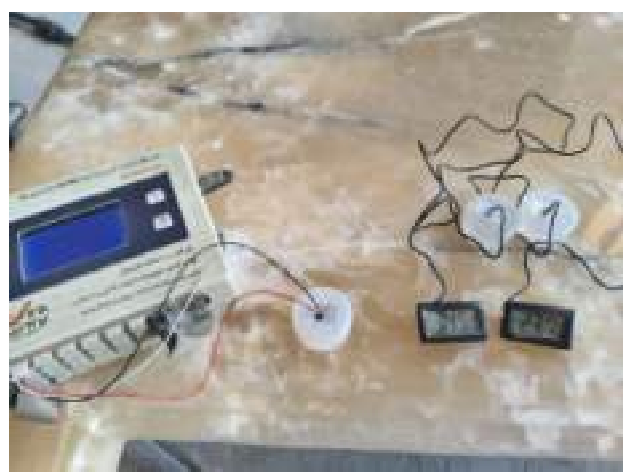

Fig. 4. Determining PCM's melting and freezing points.

Fig. 3. Salt hydrate used as the PCM (a) before and (b) after melting.

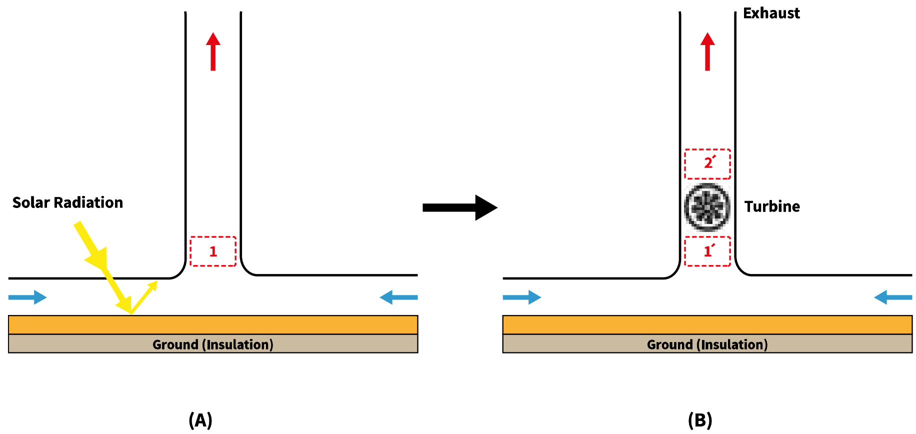

Fig. 5. Solar chimney schematic with theoretical turbine.

(EES) platform, selected for its reliable thermodynamic property functions and a sophisticated iterative matrix-solving technique. The following served as the initial benchmarks for developing the models:

- The air follows ideal gas behavior, and the transparent layers are slender.
- The flow has no frictional effects, as they are very small.
- Due to the exceptionally low Mach number, the consideration of kinetic energy in the flow can be disregarded.

The determination of heat transfer and work can be accomplished by utilizing a set of equilibrium equations derived from the fundamental principle of mass conservation. The general expression for the mass conservation equation is formulated as follows:

$$\dot{m}_i = \dot{m}_o = \dot{m} \tag{4}$$

The mass flow rates of the air entering and leaving the system are denoted by $\dot{m}_i$ and $\dot{m}_o$ $\left(\frac{kg}{s}\right)$.

The first step was to compute the mass flow rate of air in the systems with and without PCM to allow a more detailed analysis of the effect of introducing a theoretical turbine on the results. Fig. 6 depicts the methodology flowchart employed in solving the models formulated on the EES platform.

Initially, considering air as an ideal gas, the mass flow rate is determined for both solar chimneys in the absence of a turbine. It is important to note that the sensors provide accurate readings for the air's pressure, temperature, and velocity.

5. Position 1 →1′

$$\rho = \frac{P}{RT} = EOS(T,P), (R = 0.287) \tag{5}$$

$$\dot{m} = \rho AV \tag{6}$$

$$A_c = 2\pi r_c h_c \tag{7}$$

$$\dot{m}_1 = \rho_1 A V_1 \tag{8}$$

$$T_1 = T_i + \frac{\alpha I_{global}}{\dot{m}\frac{C_{p_i}}{A_r} + U} \tag{9}$$

$$P_1 = P_i + \left(\frac{\dot{m} q_{SCP}}{2\pi h_r^2 \rho_i C_{p_i} T_i}\right) \ln\left(\frac{r_r}{r_c}\right) - \dot{m}^2 \frac{\frac{1}{A_1^2} - \frac{1}{A_c^2}}{2\rho_i} \tag{10}$$

By integrating the equations governing momentum, continuity, and energy in the flow under the roof, as described in [40], we obtain equation (10). Assuming a completely subsonic flow regime with very low Mach numbers and constant values for mass flow rate, specific heat capacity and solar radiation flux are the foundations of this calculation [41]. Thus, Equation (10) can be readily obtained within the confines of these specified conditions.

After the installation of the theoretical turbine, there has been a modification in the air velocity, denoted as V1′, and the pressure entering the turbine is now referred to as P1′. It is assumed that the process from state 1 to state 1′ is isentropic, using an ideal gas. Relation (11) is derived from the application of the second law of thermodynamics under the assumption of isentropic processes. In this context, an estimation is made at P1′, and based on this assumption, T1′ is calculated.

$$\frac{P_{1'}}{P_1} = \left(\frac{T_{1'}}{T_1}\right)^{\frac{k-1}{k}}, (k = 1.4) \tag{11}$$

Knowing the value of $\dot{m}_1$ and hence V_1 in relation (8), allows you to determine V1′ using relation (12).

$$\delta q + \delta w = dh + dke \rightarrow \delta q = 0 \rightarrow \int_1^2 d(Pv) = \int_1^2 dh + \int_1^2 dke$$

$$\rightarrow P_{1'} v_{1'} - P_1 v_1 = c_{po}(T_{1'} - T_1) + \left(\frac{V_{1'}^2}{2} - \frac{V_1^2}{2}\right)$$

$$P_{1'} \frac{RT_{1'}}{P_{1'}} - P_1 \frac{RT_1}{P_1} = c_{po}(T_{1'} - T_1) + \left(\frac{V_{1'}^2}{2} - \frac{V_1^2}{2}\right)$$

$$R(T_{1'} - T_1) = c_{po}(T_{1'} - T_1) + \left(\frac{V_{1'}^2}{2} - \frac{V_1^2}{2}\right) \tag{12}$$

$$\dot{m}_{1'} = \rho_1 A V_{1'} \tag{13}$$

Position 1′→2′

Using the following equations, the thermodynamic properties at positions 2′ and exhaust can be determined iteratively.

$$\frac{T_{2'}}{T_{1'}} = \left(\frac{P_{2'}}{P_{1'}}\right)^{\frac{\gamma-1}{\gamma}} \tag{14}$$

$$\rho_{2'} = \frac{P_{2'}}{RT_{2'}} \tag{15}$$

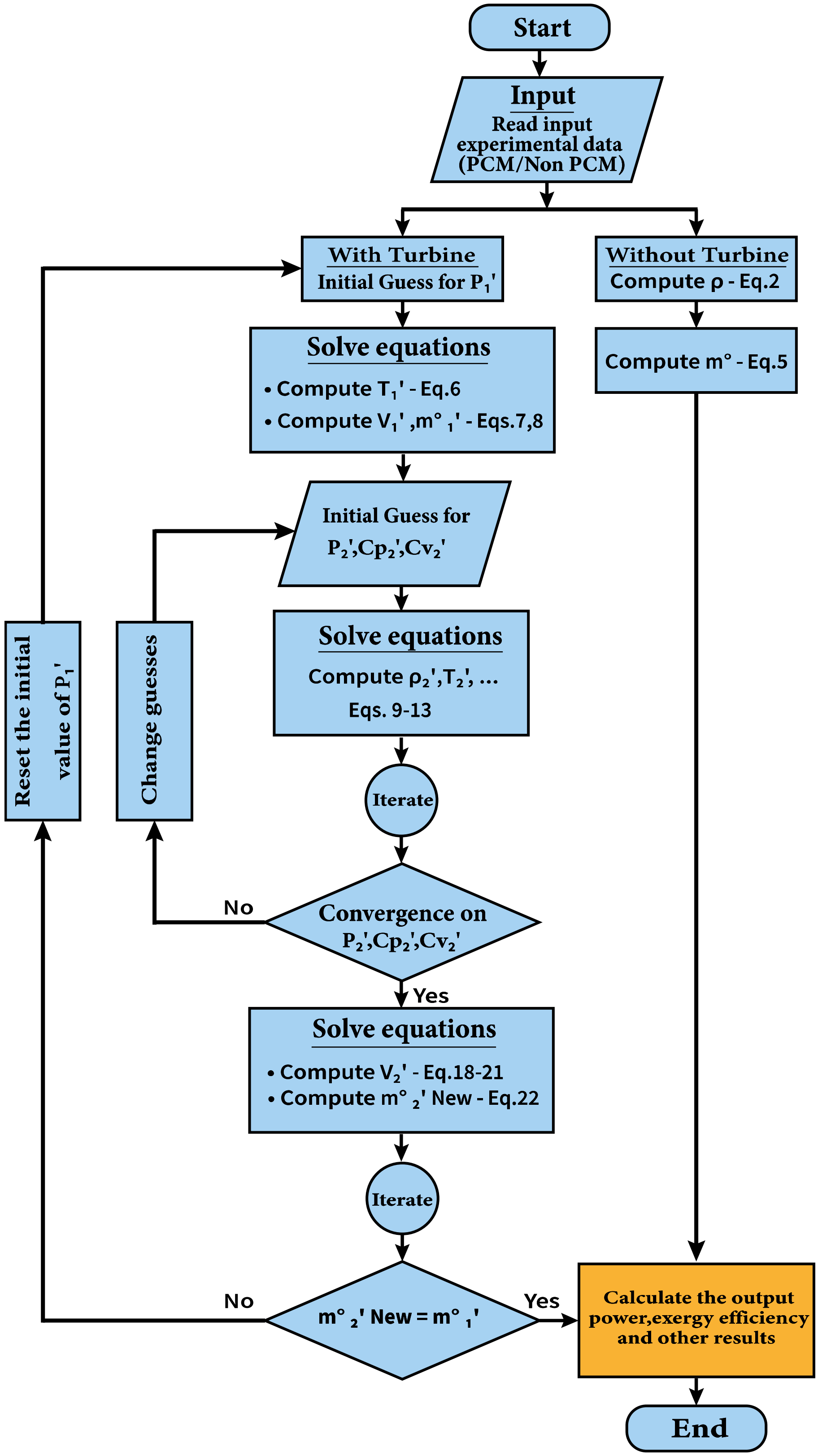

Fig. 6. EES model solution flowchart for a developing solar updraft power plant.

$$T_{Exh-ch} = T_{2'} - \left(\frac{gh_c}{C_{p_{2'}}}\right) \tag{16}$$

$$\rho_{Exh-ch} = \frac{P_{Exh-ch}}{RT_{Exh-ch}} \tag{17}$$

$$P_{2'} = P_{Exh-ch} + 0.5gh_c(\rho_{2'} + \rho_{Exh-ch}) + \left(\frac{\dot{m}}{A_c}\right)^2 \left(\frac{1}{\rho_{Exh-ch}} - \frac{1}{\rho_{2'}}\right) \tag{18}$$

Contemplate the surrounding atmospheric air external to the solar chimney system; maintaining hydrostatic equilibrium necessitates that.

$$\frac{dp}{dz} = -\rho g \tag{19}$$

The formulation for the dry adiabatic temperature lapse rate is articulated as follows, under the assumption that the air parcel behaves as an unsaturated medium undergoing gradual expansion to lower atmospheric pressure without heat exchange [42].

$$T = T_\infty - \frac{g}{c_p} z \tag{20}$$

Substituting Eq. (20) into Eq. (19), we get $P_{Exhoust-ch}$ [43] for the ambient air, assuming it obeys the ideal gas equation of state.

$$P_{Exh-ch} = P_\infty \left(1 - \frac{g}{c_p T_\infty} h_{chimney}\right)^{\frac{c_p}{R}} \tag{21}$$

$$V_{Exh-ch} = \frac{\dot{m}}{\rho_{Exh-ch} A_{chimney}} \tag{22}$$

Here, γ represents the specific heat capacity ratio. For the solution of the preceding equations, initial values for $P_{2'}$, $Cp_{2'}$ and $Cv_{2'}$ were established, and equations (14) – (18) were iteratively solved until convergence was reached within the required tolerance of 0.001.

The calculation of ventilation power is determined by the following formula [44]:

$$\dot{W}_{turbine} = \Delta P_\nu \times \dot{V}_1 \tag{23}$$

$$\Delta P_\nu = P_{1'} - P_{2'} \tag{24}$$

$$\dot{V}_4 = \frac{\dot{m}_a}{\rho_{2'}} = \dot{m}_a \times \frac{R \times T_{2'}}{P_{2'}} \tag{25}$$

The following relation depicts the turbine momentum:

$$\dot{m}_{2'} V_{2'} - \dot{m}_{1'} V_{1'} = \frac{2W_t^o}{(V_{1'} + V_{2'})} \tag{26}$$

According to this study, the turbine can be modeled as a Rankine-Froude actuator disc [45]. This actuator disc model relies on the following set of assumptions:

- A steady and homogeneous airflow.
- Uniform flow velocity at disc.
- The static pressure exhibits a discontinuous reduction across the disc.
- There is no rotational flow generated by the disc.

Given the value of V1′ in equation (26) and the value of W_t^o, it is feasible to determine V2′.

Having P2′ and T2′, the density of turbine outlet air ($\rho_{2'}$) is calculated from relation (14). Then $\dot{m}_{2'New}$ is calculated from relation (27). If $\dot{m}_{2'New}$ equals $\dot{m}_{1'}$, the initial guess (P1′) is correct; otherwise, the initial guess should be corrected and continued until the mass flow is equal.

$$\dot{m}_{2'New} = \rho_{2'} A V_{2'} \tag{27}$$

5.1. Exergy analyses

The exergy of a system denotes the maximum theoretically attainable useful work as the system converges towards equilibrium with a reference environment, characterized as an idealized system. Exergy analysis stands out as a highly effective method for balancing exergy in thermal systems due to its adept identification of irreversibilities and losses within each component. This capability is imperative as some exergy is inevitably lost owing to the irreversibility inherent in real processes. Exergy serves as a metric of energy quality, indicating its capacity to perform meaningful work. Additionally, it establishes a direct correlation between the thermodynamic state of a system and its intrinsic ability to generate productive work, providing invaluable insights into system functionality. Founded on the principles of energy conservation, the exergy balance for the system is articulated as follows:

$$\sum \dot{E}\chi_{in} - \sum \dot{E}\chi_{out} = \sum \dot{E}\chi_{lost} \tag{28}$$

The exergy balance equation is as follows:

$$E_{Lost} = Ex_{in} - Ex_{out} + Ex_{heat} - Ex_{work} \tag{29}$$

Eqs. (30) and (31) can be used to simplify the exergy of mass flows under the conditions of no humidity in the air flow and constant pressures at the intake, outflow, and ambient. The environment is thought to be in a dead state. So, 280 K was assumed to be the dead state temperature (T_{ds}).

$$E_{x_{in}} = \dot{m}c_p \left[(T_{in} - T_{ds}) - T_{ds} \left(ln \frac{T_{in}}{T_{ds}} \right) \right] \tag{30}$$

$$E_{x_{out}} = \dot{m}c_p \left[(T_{out} - T_{ds}) - T_{ds} \left(ln \frac{T_{out}}{T_{ds}} \right) \right] \tag{31}$$

The exergy flow rate arising from heat transfer is presented as:

$$Ex_{heat} = \left(1 - \frac{T_{ds}}{T_{ground}}\right) Q \tag{32}$$

The overall energy equilibrium is expressed by the equality of total energy inputs and total energy outputs:

$$\sum \dot{E}_{in} = \sum \dot{E}_{out} \tag{33}$$

$$\dot{Q} = \dot{m}_{ao}\left(h_{ao} + \frac{V_{ao}^2}{2}\right) - \dot{m}_{ai}\left(h_{ai} + \frac{V_{ai}^2}{2}\right) \tag{34}$$

In accordance with the first law of thermodynamics, $\dot{Q}$ signifies the heat transfer rate through the earth. Here, h_{ai} and h_{ao} denote the specific enthalpy of the inlet and outlet air, respectively, while V_{ai} and V_{ao} represent the inlet and outlet air velocities.

The total exergy ratio of output to input is equal to exergy efficiency:

$$\varepsilon = \frac{\dot{E}\chi_{out}}{\dot{E}\chi_{in}} \tag{35}$$

6. Results and discussion

6.1. Hourly temperature trends across Multiple days

Fig. 7 illustrates the weekly trends in hourly variations of both systems' inlet and outlet air temperatures. Tests were conducted in August and September 2022. Both systems have clear resemblances in temperature trends between the inlet and outlet airflow over these successive days. For a more detailed analysis of the behavior of both study systems, the focus is narrowed to the 24-hour timeframe within this dataset.

6.2. Validation results

A comparative analysis was conducted between the SCPP model and empirical data derived from a prototype established in Manzanares, Spain. The dataset collected on September 2nd, 1982, from a pilot plant was designated as Haaf Experimental Data and is cited as Haaf (1984) [2]. The operational parameters, including ambient temperature and pressure, for this experimental series are delineated in Table 5.

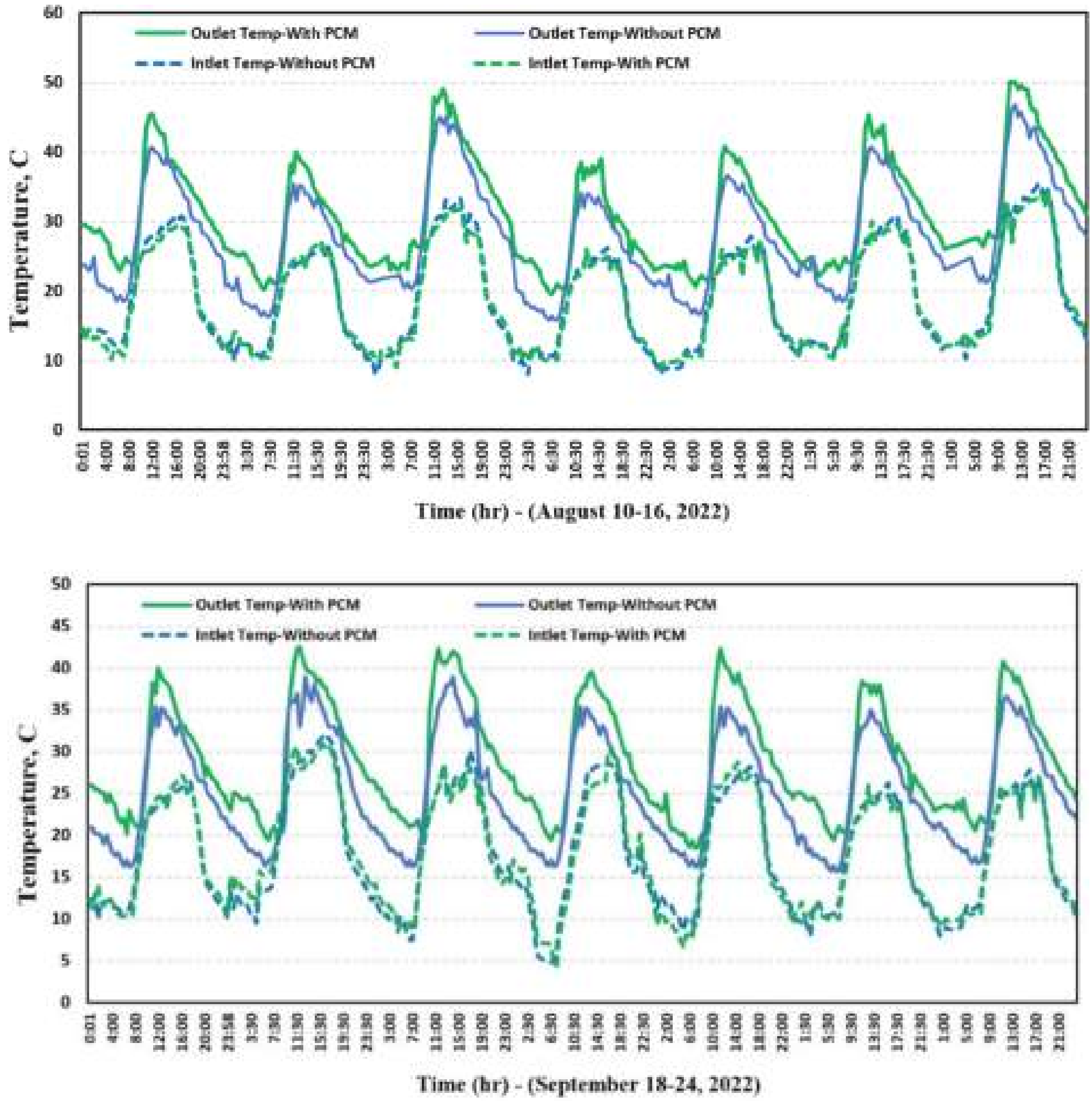

Fig. 7. Temperature hourly recorded data over the course of several days.

The updraft turbine power ($W_{turbine}$) was compared with the EES model developed for SCP using 19 data points extracted from Haaf Experimental Data from 8:00AM to 5:00PM in 30-minute intervals. As illustrated in Fig. 8, the examination of the primary output, turbine power, reveals a substantial concordance between theoretical predictions and empirical observations (Haaf Exp Data). The majority of data points within the Haaf experimental dataset were observed to lie within the range of ± 15 %.

6.3. Detailed analysis of 24-Hour system data

Our study focused on analyzing data from both systems over a 24-hour period, encompassing both day and night conditions. Fig. 9 illustrates the inlet and outlet airflow temperatures recorded on August 10, 2022, providing a comprehensive understanding of the daily behavior of both configurations, with and without the incorporation of PCM. While the displayed image represents a single measurement instance, it serves as a targeted visualization to grasp the complex processes within the system during this specific timeframe.

As anticipated, the inlet temperature exhibited consistent values in both systems. Starting at 15 °C at midnight, it decreased to 10 °C at 07:00, followed by a gradual increase to 32 °C throughout the day. Notably, there was a significant acceleration in temperature rise between 16:00 and 19:00, followed by a gradual deceleration until midnight. Comparative analysis indicated minimal temperature differences between conditions with and without PCM. However, from 00:00 to 09:00, the presence of PCM led to a decrease in the output airflow temperature from 30 °C to 25 °C. Subsequently, a substantial increase occurred, reaching around 46 °C. At 13:00, a noticeable decrease in the outlet temperature was observed, as depicted in Fig. 9. These temperature fluctuations can be attributed to variations in irradiance throughout the day, characterized by an increase from 08:00 to 13:00, followed by a

Table 5
Haaf Exp Data's input parameters were based on (Haaf, 1984) [2].

Time	T_a-[K]	ΔT_{a1}-[K]	P_a-[Pa]	$\eta_{turbine}$- [-]	I_{global}- [W/m^2]
8:00	288.2	6.3	92,930	0.85	413.8
8:30	289.9	10.3	92,930	0.85	518.5
9:00	291.8	12.2	92,930	0.85	603
9:30	292.7	13.3	92,930	0.85	687
10:00	294.1	14.8	92,930	0.85	740
10:30	294.8	15.2	92,930	0.85	781.2
11:00	296.6	15.4	92,930	0.85	816.1
11:30	297.1	15.8	92,930	0.85	838.9
12:00	296.4	17.8	92,930	0.85	850
12:30	297.8	15.5	92,930	0.85	853.6
13:00	298	15.9	92,930	0.85	831.9
13:30	298.8	17.2	92,930	0.85	803.6
14:00	299.1	17.4	92,930	0.83	750
14:30	299.9	16	92,930	0.85	699.5
15:00	299.9	14.7	92,930	0.85	633.2
15:30	300.4	12.7	92,930	0.85	544.4
16:00	300.9	11.3	92,930	0.85	420
16:30	300.5	8.1	92,930	0.85	347
17:00	300.1	7.3	92,930	0.85	245

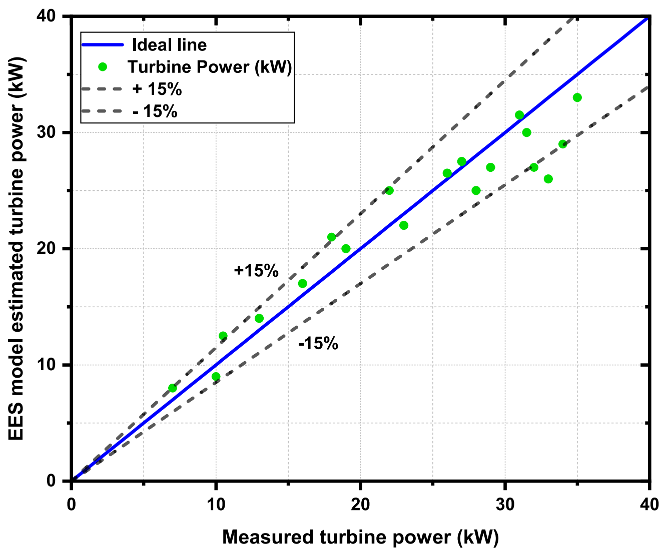

Fig. 8. EES model turbine power ($W_{turbine}$) validated against Haaf et al. dataset.

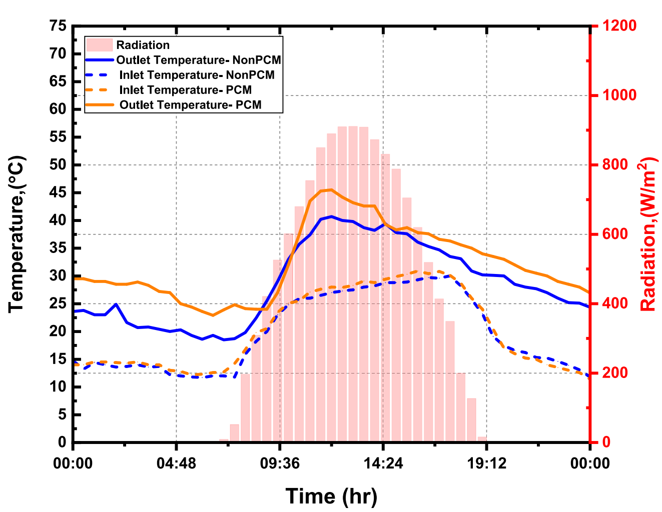

Fig. 9. Daytime inlet and exhaust air temperatures for the two cases with and without PCM.

subsequent decrease from 13:00 to 19:00.

Fig. 9 can be analyzed in terms of the temperature differential between the outlet and inlet of the system (outlet–outdoor). This analysis can provide a more insightful interpretation of the behavior exhibited by both PCM-equipped and non-PCM systems, effectively illustrating the impact of PCM presence within the system. Therefore, Fig. 9 can be partitioned into three temporal zones, with the explanations pertaining to the behavior of both systems within each zone as follows:

- Zone 1 included the period from 00:00 to 09:00. The temperature differential between the output and input (outlet–outdoor) was higher in the presence of the PCM. However, it was minimized in the presence of the PCM at 09:00, for the PCM released the stored energy at nighttime.
- Zone 2 spanned from 09:00 to 17:00. The temperature difference began to rise at 09:00 for both cases (with and without PCM) and was maximized at 13:00, for solar radiation continued to rise during 09:00–13:00. The temperature difference then began to decline at 13:00 and continued to decline during 13:00–17:00. The temperature differences were greater in the presence of the PCM.
- Zone 3 covered the time interval from 17:00 to 00:00. The temperature difference began to rise at 18:00 due to the irradiance reduction since the collector and absorber had a higher temperature and the outlet temperature declined at a lower rate than the inlet temperature. Evidently, the outlet–outdoor temperature difference was higher in the presence of the PCM, due to the hotter collector.

The mass flow rate is an essential parameter in airflow analysis, as it signifies the potential for power production, thereby highlighting its significance. Fig. 10 visually presents the air mass flow rate values for both systems alongside the pressure drop resulting from the theoretical turbine placed within the chimney. The experimental findings depicting mass flow rates through solar chimneys, with and without the integration of PCM, are meticulously presented in the subsequent diagram. Through comprehensive calculations and the solution of associated equations, the updated mass flow rate values for both conditions featuring the theoretical turbine exhibit a persistent pattern consistent with our prior observations.

The results depicted in Fig. 10 indicate that incorporating PCM leads to a discernible increase in the air mass flow rate. It was also observed that the mass flow rate experienced an augmentation during the 00:00–09:00 timeframe in the presence of PCM, attributed to the nocturnal heat release from the PCM. The use of PCM facilitates an elevated nocturnal temperature by dissipating the heat accumulated during the day, resulting in reduced air density and subsequent improvement in airflow velocity.

Across all systems, an increase in air mass flow rate was observed with the onset of solar radiation exposure, peaking at 14:00. The decrease in irradiation corresponded to a drop in velocity. However, the inclusion of PCM led to an enhanced mass flow rate. This phenomenon can be attributed to the thermal energy released by PCM, heating the collector and subsequently reducing airflow density, thereby increasing velocity.

Between 08:30 and 10:30, it was noted that the air mass flow rate in the PCM system exhibited a somewhat lower value compared to the non-PCM system. This difference may be attributed to the lower temperatures of the collector and absorber in the PCM system during this timeframe. The phase transition of PCM resulted in a partial absorption of thermal energy from the system, leading to a decline in collector temperature and a subsequent reduction in mass flow rate. Similarly, around 19:00, the mass flow rate of the PCM system experienced a notable decrease, reaching a level equivalent to that observed in the non-PCM system.

Based on the outcomes showcased in Fig. 10, it is clear that the computed mass flow rates of air passing through the system, both with and without PCM, reveal reduced values when compared to the original

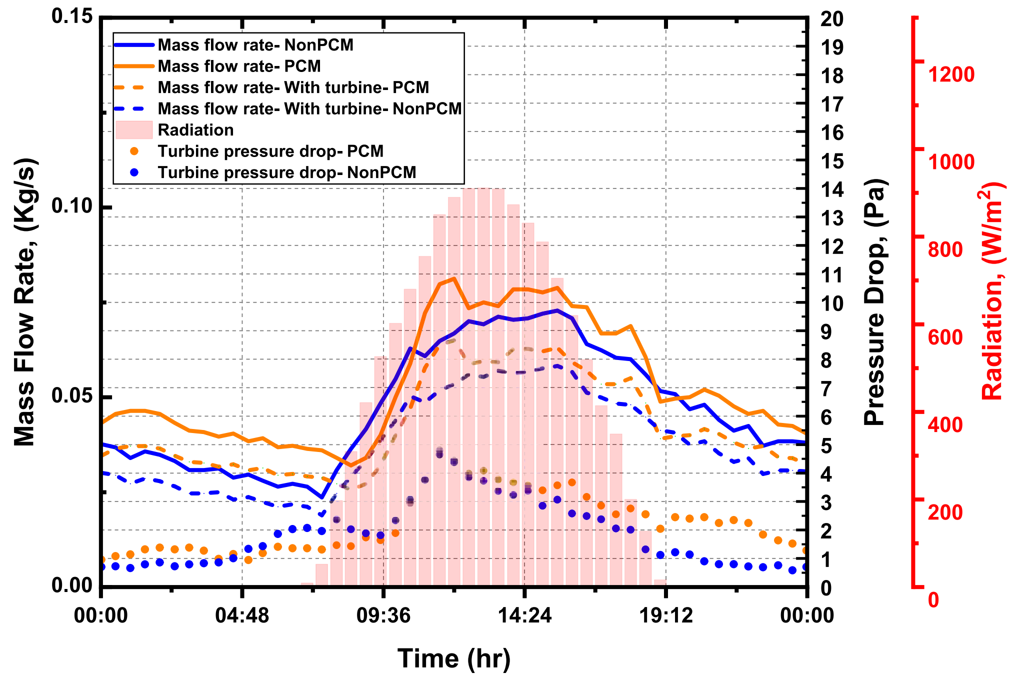

Fig. 10. Mass flow rate and pressure drop results due to the theoretical turbine.

experimental findings. This observed difference can be attributed to the inclusion of a theoretical turbine within the system framework. It is important to note that in both conditions, with and without PCM, the average daily mass flow rate of air through the system is 0.045 kg/s and 0.033 kg/s, respectively. The presented figure illustrates the pressure drop resulting from airflow passing through the turbine in the aforementioned scenarios. It is pertinent to highlight that the average pressure drops due to the passage of airflow through the turbine are 2.44 and 1.83 Pa in the presence and absence of PCM, respectively, over the course of a full day.

As can be seen in Fig. 11, the power output of the PCM-equipped system was greater than that of the non-PCM-equipped system throughout the day, except for the PCM charging hours. During the PCM charge period, the output temperature and power were lowered because some of the collector's heat was used for the phase change process. The average power output throughout the entire day for both systems, with and without PCM, is 0.16 and 0.13 Watts, respectively.

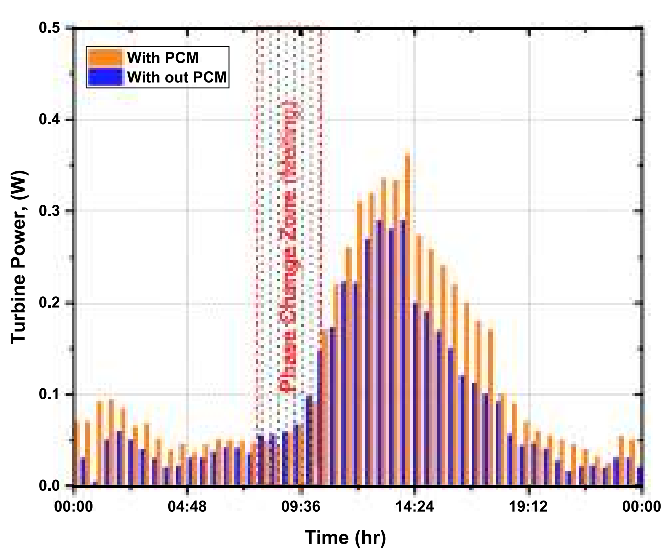

Fig. 11. Turbine power values of SCs throughout the day with and without the PCM.

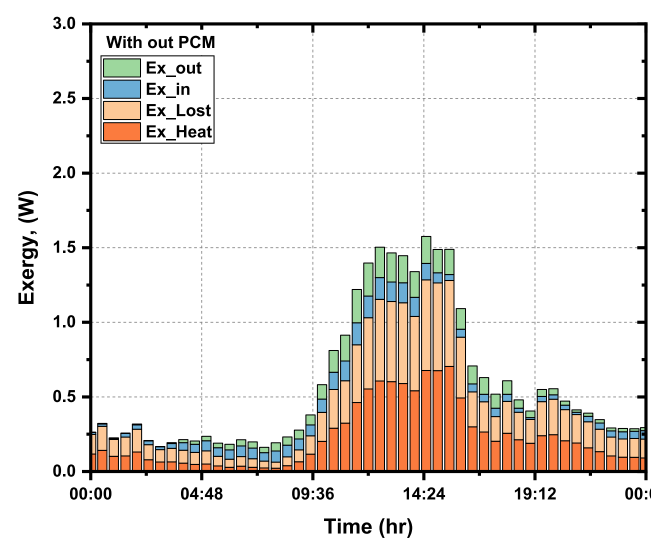

Fig. 12. The exergy rates during the day, without presence of the PCM.

According to Figs. 12 and 13, the PCM-equipped SCPP demonstrated higher exergy values compared to the non-PCM SCPP. This observation aligns with the velocity and temperature results as anticipated. The losses are considerable, especially in relation to higher levels of solar radiation, which drive increased heat transfer rates. Exergy losses peak during midday, reflecting the heightened solar radiation levels during this time. Thus, the elevated solar radiation contributes to greater exergy losses.

Fig. 14 shows the system's exergy efficiency as a significant factor. The following figure indicates that the PCM-equipped system has greater exergy efficiency throughout the day, with the exception of early morning. For the whole day, the average values for the system's exergy efficiency in the two cases with and without PCM are 0.31 and 0.25, respectively, representing a 19 % increase.

Given that heightened exergy rates arise from increased heat transfer

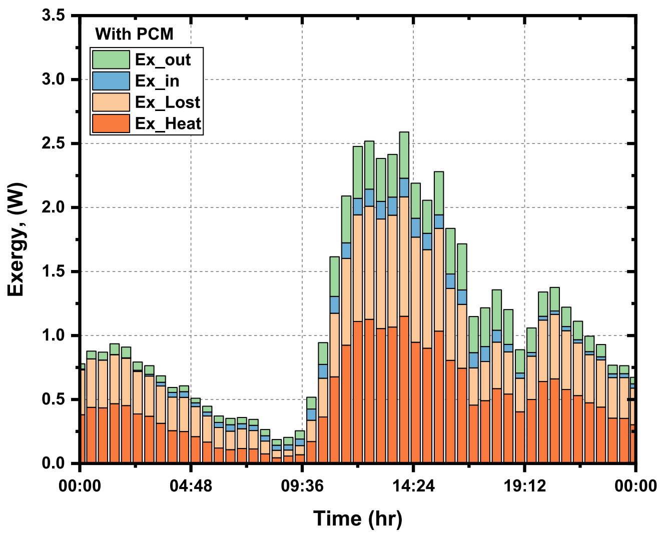

Fig. 13. The exergy rates during the day, in the presence of the PCM.

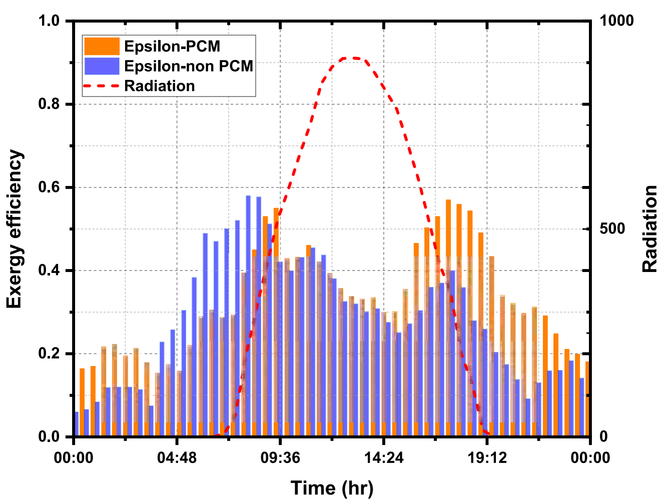

Fig. 14. Daily SC exergy efficiency with and without the presence of the PCM.

rates, augmented exergy losses and reduced exergetic efficiencies can be linked to higher levels of solar radiation. Nevertheless, it is essential to clarify that these outcomes are specific to the prototype in question, where the heat transfer rate was exclusively utilized for the removal of water from the absorber surface.

Fig. 15 compares the exergy efficiency of two systems over the course of four days. The efficiency trends observed during these four days align with the described pattern.

7. Conclusion

In this study, two prototype solar chimneys were constructed with identical specifications. Each prototype had a chimney height of 4 m and a collector diameter of 5 m. The final dimensions of the solar chimney under investigation were methodically determined, taking into consideration various parameters such as production power, cost, and structural constraints. A comprehensive elucidation of these parameters is expounded upon in a dedicated publication [38]. The air's temperature, velocity, and pressure were consistently measured and compared in both cases across a span of many days. The primary objective of this study was to examine the effect of phase change material on the daily operational efficiency of a system, utilizing empirical regional climatic data. It is notable to state that the PCM utilized in this study is a hydrated salt, which falls under the category of inorganic materials. In one of the two systems, it is employed as a thermal storage layer located beneath the collector.

To compare the performance of both systems as accurately as feasible, a theoretical turbine is assumed in the system, and all of the passing airflow characteristics for the new system are calculated, followed by an exergy analysis. To achieve this objective, one-dimensional numerical modeling was utilized in the study. In the initial phase, validation of the model relied on robust experimental data from the Manzanares pilot plant. Subsequent analysis indicated that a significant majority of data points were situated within the ± 15 % range of the experimental values, thereby affirming the accuracy and reliability of both the model and the employed methodology. Subsequently, the abovementioned modeling approach was extended to the experimental results recorded from the pilot solar chimney constructed in this investigation. Following is a summary of the results:

- Throughout most of the day, except for the PCM charge periods, the presence of the PCM resulted in a higher outlet temperature compared to when the PCM was absent. The dataset of August 10, 2022, has been selected as a representative sample within a 24-hour timeframe, and a meticulous assessment of the system's operational performance during this interval has been diligently undertaken. The temperature at the outlet reached its maximum value when the irradiance peaked at 13:00. The maximum outlet temperatures were recorded at 46 °C and 40 °C in the presence and absence of the PCM, respectively.

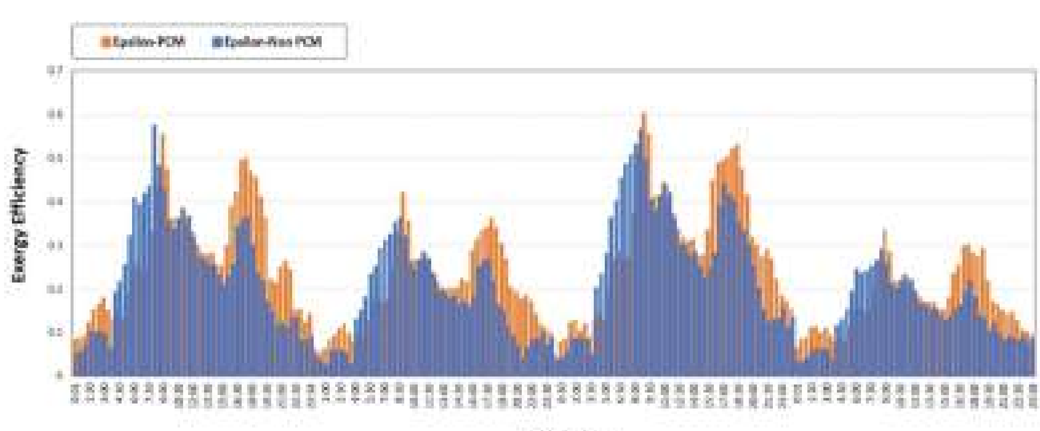

Fig. 15. Comparison of both systems' exergy efficiency over the course of 4 days.

- A theoretical turbine was integrated into the chimney during this investigation to evaluate ventilation intensity and system power output. The turbine's impact on airflow dynamics led to a decline in mass flow rate and an upswing in inlet pressure. It is significant to highlight that the daily average pressure drop in airflow was 2.44 Pa with PCM and 1.83 Pa without PCM. Moreover, the mean daily mass flow rate of air registered 0.045 kg/s with PCM and 0.033 kg/s without PCM.
- The solar chimney system equipped with PCM consistently outperformed its non-PCM counterpart in turbine production throughout the day, except during the PCM charging hours. During this specific period, a fraction of the collector's heat was directed toward the phase change process. The average daily power production of the turbine in the PCM-equipped system measured 0.16 Watts, while the non-PCM system recorded 0.13 Watts, indicating an 18 % increase in favor of the PCM-equipped system. This confirms the increased efficiency of the system due to the inclusion of PCM.
- The incorporation of PCM in the solar chimney system demonstrates higher exergy efficiency, with the exception of the early morning period. The average exergy efficiency values throughout the day are 0.31 and 0.25, representing a notable 19 % increase when PCM is utilized. These values serve as an indicative measure for compensating the system's production capacity in instances of unavailability of solar energy. Figs. 14–15 purposefully illustrate the efficacy of PCM in mitigating interruptions in power generation when solar energy is not accessible. This highlights the prospective use of PCM, presenting an opportunity for heightened system efficiency and a solution to manage interruptions in power generation during periods of restricted solar energy availability.
- Following an analysis of the system's performance within a single-day interval, the results and computations were extended to a longer timeframe to yield a more comprehensive insight into the system's operational trends. Based on the obtained results, a similar pattern of performance for this extended timeframe was identified in the system.

CRediT authorship contribution statement

Ehsan Shabahang Nia: Writing – original draft, Software, Methodology, Investigation, Data curation, Conceptualization. **Mohsen Ghazikhani:** Writing – review & editing, Visualization, Supervision, Project administration.

Declaration of competing interest

The authors declare that they have no known competing financial interests or personal relationships that could have appeared to influence the work reported in this paper.

Data availability

No data was used for the research described in the article.

References

[1] W. Haaf, K. Friedrich, G. Mayr, J. Schlaich, Solar chimneys part I: principle and construction of the pilot plant in Manzanares, Int. J. Solar Energy 2 (1) (1983) 3–20.

[2] W. Haaf, Solar chimneys: part ii: preliminary test results from the Manzanares pilot plant, Int. J. Sustain. Energ. 2 (2) (1984) 141–161.

[3] J. Schlaich, The solar chimney: electricity from the sun, Edition Axel Menges, 1995.

[4] J.R. Schlaich, R. Bergermann, W. Schiel, G. Weinrebe, Design of commercial solar updraft tower systems—utilization of solar induced convective flows for power generation, J. Sol. Energy Eng. 127 (1) (2005) 117–124.

[5] T. Ming, W. Liu, Y. Pan, G. Xu, Numerical analysis of flow and heat transfer characteristics in solar chimney power plants with energy storage layer, Energ. Conver. Manage. 49 (10) (2008) 2872–2879.

[6] S.D. Sharma, H. Kotani, Y. Kaneko, T. Yamanaka, K. Sagara, Design, development of a solar chimney with built-in latent heat storage material for natural ventilation, Int. J. Green Energy 4 (3) (2007) 313–324.

[7] G. Xu, T. Ming, Y. Pan, F. Meng, C. Zhou, Numerical analysis on the performance of solar chimney power plant system, Energ. Conver. Manage. 52 (2) (2011) 876–883.

[8] P. Guo, J. Li, Y. Wang, Y. Liu, Numerical analysis of the optimal turbine pressure drop ratio in a solar chimney power plant, Sol. Energy 98 (2013) 42–48.

[9] W. Li, P. Wei, X. Zhou, A cost-benefit analysis of power generation from commercial reinforced concrete solar chimney power plant, Energ. Conver. Manage. 79 (2014) 104–113.

[10] M. Safari, F. Torabi, Improvement of thermal performance of a solar chimney based on a passive solar heating system with phase-change materials, Energy Equipment and Systems 2 (2) (2014) 141–154.

[11] Y. Li, S. Liu, Experimental study on thermal performance of a solar chimney combined with PCM, Appl. Energy 114 (2014) 172–178.

[12] S. Nasirivatan, A. Kasaeian, M. Ghalamchi, M. Ghalamchi, Performance optimization of solar chimney power plant using electric/corona wind, J. Electrostat. 78 (2015) 22–30.

[13] E.S. Nia, M. Ghazikhani, Numerical investigation on heat transfer characteristics amelioration of a solar chimney power plant through passive flow control approach, Energ. Conver. Manage. 105 (2015) 588–595.

[14] K. Ikhlef, S. Larbi, İ. Üçgül, Experimental study of different thermal storage system effects on the performance of a small prototype solar chimney power plant, Renew. Energy 200 (2022) 516–526.

[15] L. Bin, W. Meixia, W. Qi, M. Shaoli, R. Bennacer, Effect of the position of the phase change material (PCM Na2CO3• 10H2O) on the solar chimney effect, Energy Procedia 139 (2017) 462–467.

[16] Y. Li, S. Liu, Numerical study on thermal behaviors of a solar chimney incorporated with PCM, Energy Build. 80 (2014) 406–414.

[17] H. Benli, A. Durmuş, Performance analysis of a latent heat storage system with phase change material for new designed solar collectors in greenhouse heating, Sol. Energy 83 (12) (2009) 2109–2119.

[18] R. Baby, C. Balaji, Thermal optimization of PCM based pin fin heat sinks: an experimental study, Appl. Therm. Eng. 54 (1) (2013) 65–77.

[19] M. Rezaei, M.R. Anisur, M.H. Mahfuz, M.A. Kibria, R. Saidur, I.H.S.C. Metselaar, Performance and cost analysis of phase change materials with different melting temperatures in heating systems, Energy 53 (2013) 173–178.

[20] N. Fadaei, A. Kasaeian, A. Akbarzadeh, S.H. Hashemabadi, Experimental investigation of solar chimney with phase change material (PCM), Renew. Energy 123 (2018) 26–35.

[21] L. Bin, L. Peng, M. Xiaoyan, S. Jianfei, Y. Zhaodan, Chimney effect of solar hybrid-double wall with different thickness PCM of Na2CO3• 10H2O, Energy Procedia 75 (2015) 521–526.

[22] Y. Li, S. Liu, J. Lu, Effects of various parameters of a PCM on thermal performance of a solar chimney, Appl. Therm. Eng. 127 (2017) 1119–1131.

[23] K. Bashirnezhad, S.A. Kebriyaee, A. Moosavi, The experimental appraisement of the effect of energy storage on the performance of solar chimney using phase change material, Sol. Energy 169 (2018) 411–423.

[24] P. Thantong, J. Khedari, P. Chantawong, Investigation of thermal performance by applying a solar chimney with PCM towards the natural ventilation of model house under Climate of Thailand, Mater. Today:. Proc. 5 (7) (2018) 14862–14867.

[25] M.E. Tiji, M. Eisapour, R. Yousefzadeh, M. Azadian, P. Talebizadehsardari, A numerical study of a PCM-based passive solar chimney with a finned absorber, J. Build. Eng. 32 (2020) 101516.

[26] W. Chen, Analysis of heat transfer and flow in the solar chimney with the sieve-plate thermal storage beds packed with phase change capsules, Renew. Energy 157 (2020) 491–501.

[27] M. Aligholami, S.S. Khosroshahi, A.R. Khosroshahi, Hydrodynamic and thermodynamic enhancement of a solar chimney power plant, Sol. Energy 191 (2019) 180–192.

[28] Y. Pahamli, M.S. Valipour, Application of phase change materials in refrigerator and freezer appliances: A comprehensive review, J. Heat Mass Trans. Res. 8 (1) (2021) 87–104.

[29] M.H. Shojaeefard, M. Jourabian, A.A. Rabienataj Darzi, A. Bayat, Inward melting inside a horizontal multilobed capsule with conductive wall affected by Ag-MgO/water hybrid and MgO/water nanofluids, J. Heat Mass Trans. Res. 8 (2) (2021) 205–223.

[30] L. Rezaei, S. Saeidi, A. Sápi, M.A. Senoukesh, G. Gróf, W.H. Chen, J.J. Klemeš, Efficiency improvement of the solar chimneys by insertion of hanging metallic tubes in the collector: Experiment and computational fluid dynamics simulation, J. Clean. Prod. 415 (2023) 137692.

[31] A. Atia, S. Bouabdallah, B. Ghernaout, M. Teggar, T. Benchatti, Investigation of various absorber surface shapes for performance improvement of solar chimney power plant, Appl. Therm. Eng. 235 (2023) 121395.

[32] M. Corcione, L. Fontana, A. Quintino, First analysis of a novel design of a solar chimney with absorber elements distributed in the air channel, Appl. Therm. Eng. 230 (2023) 120539.

[33] S. Yoo, S. Oh, A.A. Hachicha, Numerical simulation and performance evaluation of filter-equipped solar chimney power plants, Appl. Therm. Eng. 218 (2023) 119284.

[34] E. Abdelsalam, Z.A. El-Rub, M. Alkasrawi, D. Ibrahim, A. Azzam, T. Salameh, A. G. Olabi, A novel design of a twin-chimney solar power plant for power and distilled water production, Thermal Sci. Eng. Progress 46 (2023) 102231.

[35] S. Huang, W. Li, J. Lu, Y. Li, Z. Wang, S. Zhu, Experimental study on thermal performances of a solar chimney with and without PCM under different system inclination angles, Energy 290 (2024) 130154.

[36] H.T. Chen, C.W. Chang, S. Rashidi, J. Čespiva, W.M. Yan, Natural convection heat transfer in isosceles prismatic roof with perforated partition and phase change material, Thermal Sci. Eng. Progress 48 (2024) 102428.
[37] J. Kim, S. Lee, J. Park, J.Y. Park, Potential need for vestibule structures in solar updraft tower, Thermal Sci. Eng. Progress 47 (2024) 102332.
[38] E.S. Nia, M. Ghazikhani, Dimensional investigation of solar chimney power plant based on numerical and experimental results, Thermal Sci. Eng. Progress 37 (2023) 101548.
[39] L. Kirkup, R.B. Frenkel, An introduction to uncertainty in measurement: using the GUM (guide to the expression of uncertainty in measurement), Cambridge University Press, 2006.
[40] T. Chitsomboon, A validated analytical model for flow in solar chimney, Int. J. Renewable Energy Eng. 3 (2) (2001) 339–346.
[41] A. Koonsrisuk, T. Chitsomboon, Mathematical modeling of solar chimney power plants, Energy 51 (2013) 314–322.
[42] J.G. Calvert, Glossary of atmospheric chemistry terms (Recommendations 1990), Pure Appl. Chem. 62 (11) (1990) 2167–2219.
[43] A. Koonsrisuk, Mathematical modeling of sloped solar chimney power plants, Energy 47 (1) (2012) 582–589.
[44] M. Mehrpooya, M. Shahsavan, M.M.M. Sharifzadeh, Modeling, energy and exergy analysis of solar chimney power plant-Tehran climate data case study, Energy 115 (2016) 257–273.
[45] Eggleston, D. M., & Stoddard, F. (1987). Wind turbine engineering design.
[46] Li, Y. (2013). Thermal performance analysis of a PCM combined solar chimney system for natural ventilation and heating/cooling (Doctoral dissertation, Coventry University).
[47] S. Liu, Y. Li, Heating performance of a solar chimney combined PCM: a numerical case study, Energy Build. 99 (2015) 117–130.
[48] Y. Li, S. Liu, A. Shukla, Experimental analysis on use of thermal conductivity enhancers (TCEs) for solar chimney applications with energy storage layer, Energy Build. 116 (2016) 35–44.
[49] A.A. Ismaeel, H.H. Al-Kayeim, A.T. Baheta, M.A. Aurybi, Comparative critique of thermal energy storage technique in solar chimney power plants, Int. Energy J. 16 (1) (2016).
[50] T. K Murtadha, H. M Salih, A. D Salman, Experimental and numerical study of closed loop solar chimney assisted with PCM and CFM as thermal energy storage collector, Eng. Technol. J. 34 (13A) (2016) 2450–2463.
[51] J.F. Dordelly, M. Coillot, M. El Mankibi, R. Enriquez, M.J. Jimenez, J.A. Landa, Active Solar Chimney (ASC)-Numerical and experimental study of energy storage and evaporative cooling, World Sol. Congr, Abu Dhabi, 2017.
[52] J.C.F. Dordelly, M. El Mankibi, M. Coillot, in: November). Numerical and Experimental Investigations of a PCM Integrated Solar Chimney, IEEE, 2018, pp. 1–6.
[53] J.C.F. Dordelly, M. Coillot, M. El Mankibi, R.E. Miranda, M.J. Jimenez, J.A. Landa, Numerical and Experimental Assessment of a PCM Integrated Solar Chimney, Int. J. Energy Environ. Eng. 12 (4) (2018) 252–258.
[54] J. Xamán, R. Vargas-López, M. Gijón-Rivera, I. Zavala-Guillén, M.J. Jiménez, J. Arce, Transient thermal analysis of a solar chimney for buildings with three different types of absorbing materials: Copper plate/PCM/concrete wall, Renew. Energy 136 (2019) 139–158.
[55] N. Ochiai, K. Sagara, T. Yamanaka, H. Kotani, Y. Momoi, Y. Kaneko, Numerical Simulation of Natural Ventilation Performance of Solar Chimney with Built-in Phase Change Material, Proceedings of Advanced Building Ventilation and Environmental Technology for Addressing Climate Change Issues 1 (2011) 207–212.
[56] S. Rashidi, J.A. Esfahani, E. Hosseinirad, Assessment of solar chimney combined with phase change materials, J. Taiwan Inst. Chem. Eng. 124 (2021) 341–350.